
A novel method for slip prediction of walking biped robots

Iyad Hashlamon, Mehmet Mert Gülhan, Orhan Ayit and Kemalettin Erbatur

Robotica / *FirstView* Article / November 2015, pp 1 - 21
DOI: 10.1017/S0263574715000818, Published online: 03 November 2015

Robotica: page 1 of 21. © Cambridge University Press 2015
doi:10.1017/S0263574715000818

A novel method for slip prediction of walking biped robots

Iyad Hashlamon†*, Mehmet Mert Gülhan‡, Orhan Ayit‡ and Kemalettin Erbatur‡

†*Palestine Polytechnic University, Hebron, Palestine*
‡*Faculty of Engineering and Natural Sciences, Sabanci University, Tuzla, Istanbul, Turkey. E-mails: mertgulhan@sabanciuniv.edu, orhanayit@sabanciuniv.edu, erbatur@sabanciuniv.edu*

(Accepted September 21, 2015)

SUMMARY
This paper proposes a new approach for slip prediction of walking biped robots. The slip prediction is a measurement-based and friction behavior-inspired approach. A measurement-based online algorithm is designed to estimate the Coulomb friction which is regarded as a slip threshold. To predict the slip, a safety margin is introduced in the negative vicinity of the estimated Coulomb friction. The estimation algorithm concludes that if the applied force is outside the safety margin, then the foot tends to slip. The proposed approach depends on the available type of measurements. Three options of measurements are discussed. Among them, the foot acceleration and ankle force measurements scenario is validated by experiments on the humanoid SURALP (Sabanci University Robotics Research Laboratory Platform). The results demonstrate the effectiveness of the proposed approach for slip prediction and detection.

KEYWORDS: Biped; Slip prediction; Slip detection; Friction; LIPM and CoM states estimation.

1. Introduction

Balance preserving of the biped robot while walking is a complicated task. Generally, bipedal walking depends on generated stable trajectories. The linear inverted pendulum model (LIPM) is widely used for walking trajectory generation.[1] As a stability criterion, the Zero Moment Point (ZMP) stability criterion[2,3] is widely employed. However, even when stable walking trajectories are employed, the robot may tend to tip over in real life. This is because of environmental uncertainty and changes. Therefore, robot adaptation to ground conditions is highly desirable.

Foot contact with the environment poses a critical problem. The robot foot, when it is in contact with the ground, is subjected to distributed reaction forces due to the interaction between the foot sole and the contact surface. The horizontal components of these forces represent the friction forces that facilitate biped walking and locomotion. These friction forces constrain the balance of the biped walker.[4,5] Further, the friction forces determine the maximum acceleration and deceleration that the robot can achieve, and hence the maximum forces allowed to be applied to the robot.[6,7] If the forces or torques applied by the robot legs exceed certain thresholds, then the biped might lose its stability.[7] However, determining these friction forces is a challenge.

Researchers conducted experiments on walking on arbitrary surfaces, and with arbitrary coefficients of friction. In mass of the studies, the coefficient of friction μ is considered to be known. In real life, however, μ is unknown or is only inaccurately known. Assuming a too high value of μ may lead to foot slipping. On the other hand, low value constrains the motion conservatively.

Slip is defined as the phenomenon when the relative velocity between the foot of the biped robot and the contact surface is not zero when the foot is in contact. This leads to define the slip force as the difference between the total forces applied at the foot and the friction forces. These friction forces

* Corresponding author. E-mail: iyad@ppu.edu, hashlamon@sabanciuniv.edu

can be measured directly using sensors embedded at the feet of the humanoid robot[8,9] or indirectly based on other measurements like foot ankle forces and foot acceleration. Slip forces, however, are not measured directly, they are computed.

1.1. Related work

Although slip prediction is a valuable asset and significant in preventing the biped robot from falling, only a few studies were reported. Often, no slip contacts are assumed in bipedal walking. In other words, μ is either considered to be very high[10–13] or accurately known.[14] Then, the maximum applied torques are constrained accordingly.[15,16] Control approaches were designed to compensate for the applied forces and torques when they exceed the constraints.[17,18] For the single support phase of the biped robot, a method for calculating the slipping forces and predicting their most possible slipping direction is proposed.[5] However, a known friction coefficient assumption is impractical and the environment changes a lot (the walking surface varies a lot during the walk). A method for slip detection is proposed for an unknown floor coefficient of friction.[19] This method depends on enlarging the walking step gradually until the biped slips which is used later as an upper limit for the trajectory planning. However, this requires several steps to learn the limit.

Without using the coefficient of friction, a slip observer is introduced to detect the slip and estimate the slipping force.[20] The difference between the desired reaction force and the measured reaction force is regarded as the slipping force. The desired force is calculated using the 3D LIPM with known ZMP. However, the desired reaction force does not include the external and inertial forces. Therefore, the slipping force is not necessarily due to higher desired reaction forces, and the slip may occur even the desired reaction force is less than the measured.

Measurement-based methods are developed for slip detection. For a quadruped during the supporting phase, a slip detection method is introduced based on the quadruped leg acceleration (obtained from an accelerometer).[21] The introduced method detects the slip when the integration of the acceleration exceeds certain threshold. For slip-related falls, intelligent shoes were introduced for slip detection.[22] The principle depends on the human postural instability based on information from in-shoe pressure sensors and optional rate gyros. Another slip detection method for bipeds is proposed based on an insole sensor system, it utilizes force and acceleration measurements.[23] The detection algorithm is: slipping exists when the force and acceleration readings are larger than certain thresholds, otherwise there is no slip. Slip is also detected by searching in the acceleration signal for high amplitudes before, during and after the slip spike.[24] In the same contest, the acceleration and gyro readings with unscented Kalman filter UKF are used for slip detection, here the UKF innovation is used for detecting the slip.[25] For slow walking bipeds, the biped body acceleration is utilized through simplified models to calculate the applied forces at the foot. Then, the slip is detected by comparing the calculated applied forces with the measured forces from force sensors assembled at the foot sole.[26] However, the previous works are for slip detection not prediction.

Friction model-based methods with identified model parameters are employed for slip prevention.[27,28] However, friction modeling is a challenge since the friction behavior is highly nonlinear. Moreover, the friction at low velocities and the stiction friction pose more challenges.

1.2. Problem definition

Slip may cause the robot to tip over. Therefore, it has a critical importance. Although some studies are reported to compensate for the slip, they in general work when slip occurs. Beyond this, using friction models for slip prevention poses problems due to the nonlinear and complex behavior of the friction.

Measurement-based method is fruitful since it does not use friction models (friction model-free) and thus it avoids friction modeling problems. The idea of this paper is that slip can be predicted by developing a measurement-based online adaptive algorithm that utilizes certain measurements. This algorithm must be able to estimate the friction between the foot and the ground, predict the slip ahead and overcome the challenges of the friction behavior. However, since this algorithm is measurement-based, at least two measurements are required at the foot. The options for the two measurements are: (1) ankle forces and foot accelerations, (2) ankle forces and reaction forces at the foot sole, or (3) acceleration of the robot body and the reaction forces at the foot sole. For the last case, a model of the biped is required too.

1.3. The proposed method and contribution

By knowing the walking surface friction parameters, the biped walking can adapt its motion so that it preserves its stability. Therefore, this paper is motivated to develop an online friction estimation algorithm for walking bipeds.

Here, based on the friction behavior, an online measurement-based algorithm is designed to estimate the Coulomb friction. This algorithm updates the estimated friction online adaptively. Based on the friction behavior, the Coulomb friction is the minimum friction beyond which slip will be observed. Therefore, it is used to decide whether the foot is going to slip or not. This is achieved by considering the Coulomb friction as a slip threshold. To predict the slip, a safety margin is subtracted from the Coulomb friction to define a slip risk band. Hence, whenever the applied force is below this band, it is assumed that the foot will not slip. If the applied force is within the safety margin, then the foot tends to slip. Finally, if the applied force is larger or equal to the Coulomb friction, it is concluded that the foot slips. Different measurement scenarios are discussed. The experiments are based on the foot acceleration and ankle force measurements according to the available measurements.

The contribution of this paper is developing an online friction behavior-inspired algorithm for slip prediction. This algorithm is adaptive, measurement-based, and can estimate the Coulomb, static and Stribeck friction between the foot and the contact surface. Moreover, the paper proposes a method for computing the reaction forces at the foot based on the measured biped body acceleration and foot reaction forces. The measured and computed foot reaction forces are used for slip detection.

The rest of the paper is organized as follows: Section 2 introduces the friction. Slip is defined in Section 3. The slip detection and prediction approaches are shown in Section 4 and Section 5 respectively. Section 6 presents the results. The paper conclusion is in Section 7.

2. Friction

Friction is a nonlinear and complex phenomenon under research. Researchers work on mathematical models that can describe this behavior.[29–35] Although several friction models are developed, there is no exact model that represents the friction behavior. This poses a challenge for the friction estimation and compensation. This is why online measurement-based friction estimation enters the picture. The estimation here is friction behavior-inspired method. Therefore, the friction behavior is explained here.

Consider the object in Fig. 1a, the friction force is the tangential reaction force F_f in the opposite direction of motion. The applied tangential force is F_t and the normal reaction force is $F_N \geq 0$. The Friction force F_f can be either a static force, denoted by F_{fs}, or kinetic one, denoted by F_{fd} as in Fig. 1b. These forces are respectively defined by

$$F_{fs} \leq \mu_{\text{static}} F_N, \tag{1}$$

and

$$F_{fd} = \mu_d F_N, \tag{2}$$

where μ_{static} is the static coefficient of friction and μ_d the kinetic coefficient of friction. When the object is at rest, it resists the initial motion with a larger frictional force than it does when the motion starts. This can be stated by the coefficients of friction as $\mu_{\text{static}} \geq \mu_d$. As shown in Fig. 1b, the value of F_{fs} is at its maximum when the relative motion starts, and then the friction force decreases. The maximum value of F_{fs} is denoted by F_s. At F_s, the maximum applied force called $F_{t_{\max}}$ is observed. The region where the object is in static condition of no motion ($F_t < F_s$) is referred to as the static region. The phase of motion with nonzero velocity is called the kinetic region ($F_t > F_s$). Equivalently, the allowable force F_t such that the object is in no motion must be inside a cone with radius F_s and height F_N as shown in Fig. 1c.

There is no exact model that represents the friction force. In general, the dominant friction components are the Coulomb friction F_c, Stribeck friction F_{st}, F_s and viscous friction F_v illustrated in Fig. 2.

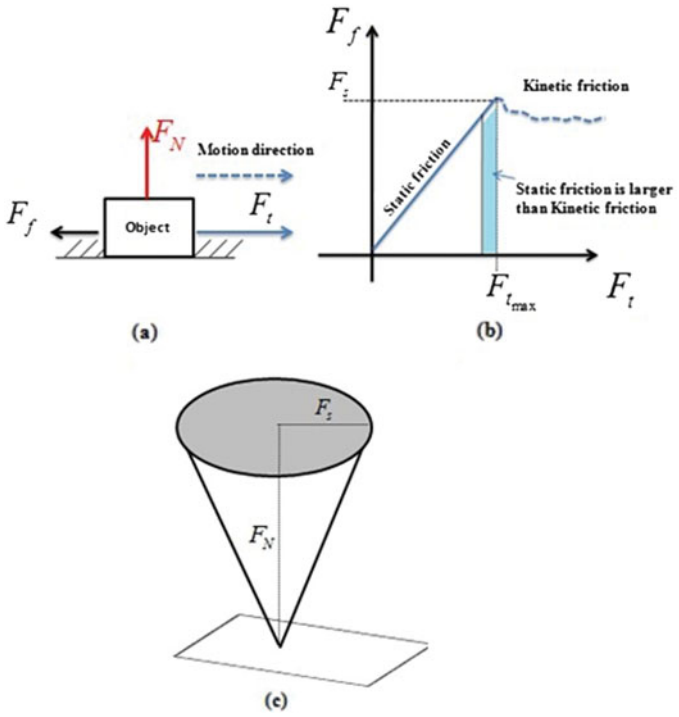

Fig. 1. (a) Object free body diagram (the object weight is in the normal force), (b) Friction force behavior, and (c) the friction cone.

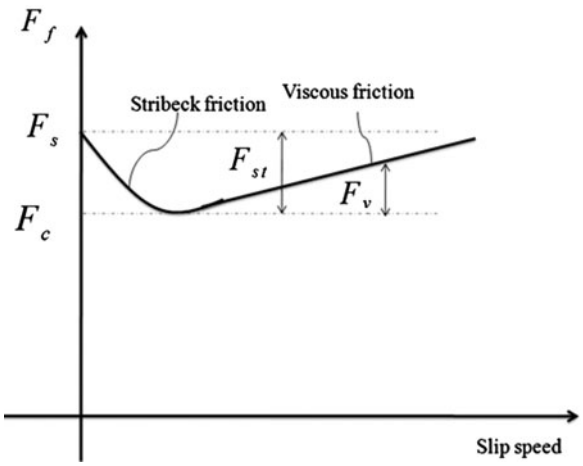

Fig. 2. Friction components.

3. Slip Definition

Consider one of the robot feet as in Fig. 3a, the total force on the foot is F. Its tangential components in the x- and y-directions are F_{t_x} and F_{t_y} respectively. The friction force components in the x- and y-directions are F_{f_x} and F_{f_y} respectively. The normal reaction force is $F_N \geq 0$. The slip is defined as the phenomenon when F_f between the foot and the contact surface is not enough to make the relative velocity between them zero. In other words, it is the phenomenon when $\|\mathbf{F}_t\| = \sqrt{F_{t_x}^2 + F_{t_y}^2} > \|\mathbf{F}_f\| = \sqrt{F_{f_x}^2 + F_{f_y}^2}$, or in terms of components, $F_{t_x} > F_{f_x}$ or/and $F_{t_y} > F_{f_y}$. This leads to generate a slip force F_{slip_x} in the x-direction or/and a slip force F_{slip_y} in the y-directions. Thus, the slip force

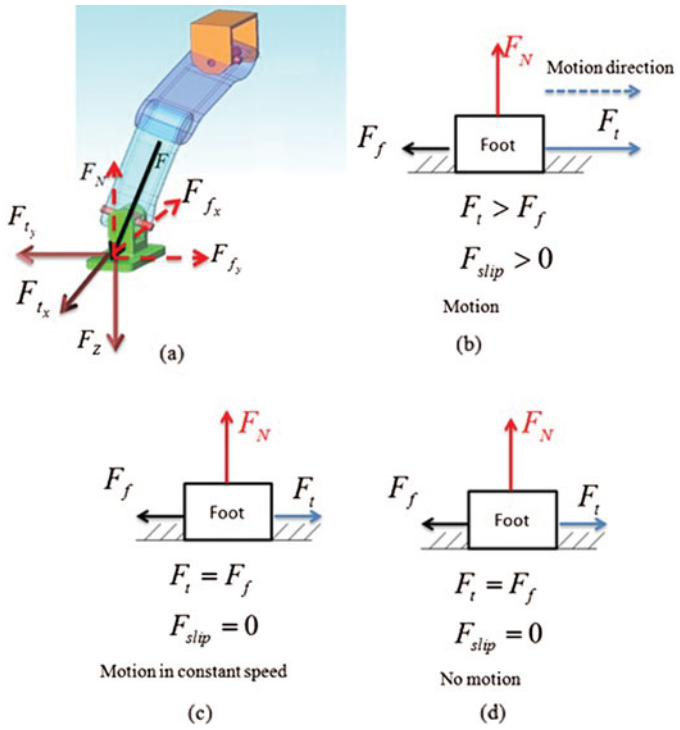

Fig. 3. Slip force conditions.

vector $\mathbf{F}_{\text{slip}} \equiv [\, F_{\text{slip}_x} \;\; F_{\text{slip}_y} \,]^T$ is stated as

$$\mathbf{F}_{\text{slip}} = \mathbf{F}_t - \mathbf{F}_f, \tag{3}$$

with $\mathbf{F}_t = [\, F_{t_x} \;\; F_{t_y} \,]^T$ and $\mathbf{F}_f = [\, F_{f_x} \;\; F_{f_y} \,]^T$.

The analysis for both x- and y-directions is the same. Therefore, for convenience, the subscriptions x and y are dropped. According to Eq. (3) $F_{\text{slip}} \geq 0$, for the case when $F_{\text{slip}} > 0$ the foot is in motion as in Fig. 3b. When $F_{\text{slip}} = 0$, it indicates that the foot is either moving at a constant speed as in Fig. 3c or the foot is static as in Fig. 3d. The situation in Fig. 3c poses a problem which will be solved by assuming that the foot was not initially moving at a constant speed.

4. Slip Detection

Slip occurrence is detected according to Eq. (3). The foot slips whenever it is subjected to a slip force $F_{\text{slip}} > 0$. Calculating F_{slip} depends on the available measurements. Here three cases are discussed.

1. Ankle forces and foot accelerations, hence $\mathbf{F}_t$ is directly measured.
2. Ankle forces and the reaction forces at the foot sole, hence $\mathbf{F}_t$ and $\mathbf{F}_f$ are directly measured.
3. Acceleration of the robot body and the reaction forces at the foot sole. For this case, a model of the biped is required too.

4.1. Slip detection with ankle forces and foot accelerations measurements

An accelerometer mounted at the foot can be measured $\mathbf{F}_{\text{slip}}$ according to

$$\mathbf{F}_{\text{slip}} = m_f \ddot{\mathbf{p}}, \tag{4}$$

where m_f is the foot mass, $\ddot{p}_x$ and $\ddot{p}_y$ the measured foot accelerations in the x- and y-directions respectively and $\ddot{\mathbf{p}} \equiv \left[\, \ddot{p}_x \;\; \ddot{p}_y \,\right]^T$. Hence, the foot slips whenever $\ddot{p} > 0$ (the subscriptions x and y are dropped). Bearing in mind that $\mathbf{F}_t$ is measured using a force/torque sensor, then the friction force is

calculated from Eqs. (3) and (4) as

$$\mathbf{F}_f = \mathbf{F}_t - m_f \ddot{\mathbf{p}}. \tag{5}$$

However, as an implementation consideration, the accelerometer generates a reading even though the biped is not moving. Therefore, slip is detected if the acceleration readings are larger than a threshold Tr (i.e. if $\ddot{\mathbf{p}} \geq Tr$). This threshold depends on the initial accelerometer reading.

4.2. Slip detection with measured friction and tangential forces

If the biped is equipped with contact force sensors at the feet soles and force/torque sensors at the ankles, then the measured $\mathbf{F}_f$ and $\mathbf{F}_t$ are used directly in Eq. (3) to detect the slip.

4.3. Slip detection with measured friction force and biped body acceleration

Referring to Eq. (3), the friction force is directly measured by force sensors located at the foot sole. $\mathbf{F}_t$ is unmeasured. However, it can be calculated based on a reduced model of the biped.

Assume that there are l force sensors at each foot. These sensors are attached to known contact points at each foot with known positions relative to the foot frame. There outputs for the right and left feet are $\mathbf{F}_{\mathbf{E_R}}$ and $\mathbf{F}_{\mathbf{E_L}}$ respectively. These measured forces are grouped into the force vector $\mathbf{F}_\mathbf{E}$ and defined as $\mathbf{F}_\mathbf{E} \equiv \left[\, \mathbf{F}_{\mathbf{E_R}}^T \quad \mathbf{F}_{\mathbf{E_L}}^T \,\right]^T$. The computed forces at the aforementioned contact points are $\bar{\mathbf{F}}_{\mathbf{E_R}}$ for the right foot and $\bar{\mathbf{F}}_{\mathbf{E_L}}$ for the left foot. These computed forces are grouped into the force vector $\bar{\mathbf{F}}_\mathbf{E} \equiv \left[\, \bar{\mathbf{F}}_{\mathbf{E_R}}^T \quad \bar{\mathbf{F}}_{\mathbf{E_L}}^T \,\right]^T$. The measured and computed force vectors are defined as

$$\mathbf{F}_{\mathbf{E_m}} = \begin{bmatrix} {}^{\mathbf{m}}F_{f_x}^1 \\ {}^{\mathbf{m}}F_{f_y}^1 \\ {}^{\mathbf{m}}F_N^1 \\ {}^{\mathbf{m}}F_{f_x}^2 \\ {}^{\mathbf{m}}F_{f_y}^2 \\ {}^{\mathbf{m}}F_N^2 \\ \vdots \\ {}^{\mathbf{m}}F_{f_x}^l \\ {}^{\mathbf{m}}F_{f_y}^l \\ {}^{\mathbf{m}}F_N^l \end{bmatrix}, \quad \bar{\mathbf{F}}_{\mathbf{E_m}} = \begin{bmatrix} {}^{\mathbf{m}}F_{t_x}^1 \\ {}^{\mathbf{m}}F_{t_y}^1 \\ {}^{\mathbf{m}}\bar{F}_N^1 \\ {}^{\mathbf{m}}F_{t_x}^2 \\ {}^{\mathbf{m}}F_{t_y}^2 \\ {}^{\mathbf{m}}\bar{F}_N^2 \\ \vdots \\ {}^{\mathbf{m}}F_{t_x}^l \\ {}^{\mathbf{m}}F_{t_y}^l \\ {}^{\mathbf{m}}\bar{F}_N^l \end{bmatrix}, \tag{6}$$

with

$$\mathbf{m} = \begin{cases} \mathbf{L} & \text{left} \\ \mathbf{R} & \text{right} \end{cases}. \tag{7}$$

where $\mathbf{F}_{\mathbf{E_m}}$ and $\bar{\mathbf{F}}_{\mathbf{E_m}}$ are the measured and computed force vectors respectively at the foot $\mathbf{m}$, ${}^{\mathbf{m}}F_{f_j}^i$ the measured friction force component in the $j = \{x- \text{or } y-\}$ direction at contact point $i = 1, 2, \ldots, l$ of the foot $\mathbf{m}$, ${}^{\mathbf{m}}F_N^i$ the measured normal force component at contact point $i = 1, 2, \ldots, l$ of the foot $\mathbf{m}$. ${}^{\mathbf{m}}F_{t_j}^i$ and ${}^{\mathbf{m}}\bar{F}_N^i$ are the computed tangential and normal force components at contact point $i = 1, 2, \ldots, l$ of the foot $\mathbf{m}$.

The computation of the tangential force depends on the biped model. The biped, which is considered here, consists of a body and two legs connected to it as in Fig. 4. Its motion is defined in the fixed world frame O_w. The body is considered as the base link with the base coordinate system O_b. The hips and feet soles have coordinate frames too.

For this work, it is assumed that the biped is equipped with contact force sensors with frame origin O_F assembled at the feet soles,[36] joint encoders attached to the joint actuators and an IMU with a frame origin O_I. The IMU is composed of 3-axes accelerometer and 3-axes rate gyro.

The biped interacts with the ground and modeled as a free-fall manipulator. For a biped with N number of joints, and the defined generalized coordinates $\mathbf{x}^T = [\mathbf{p}_b^T, \mathbf{A}_b^T, \boldsymbol{\theta}^T] \in R^3 \times SO(3) \times$

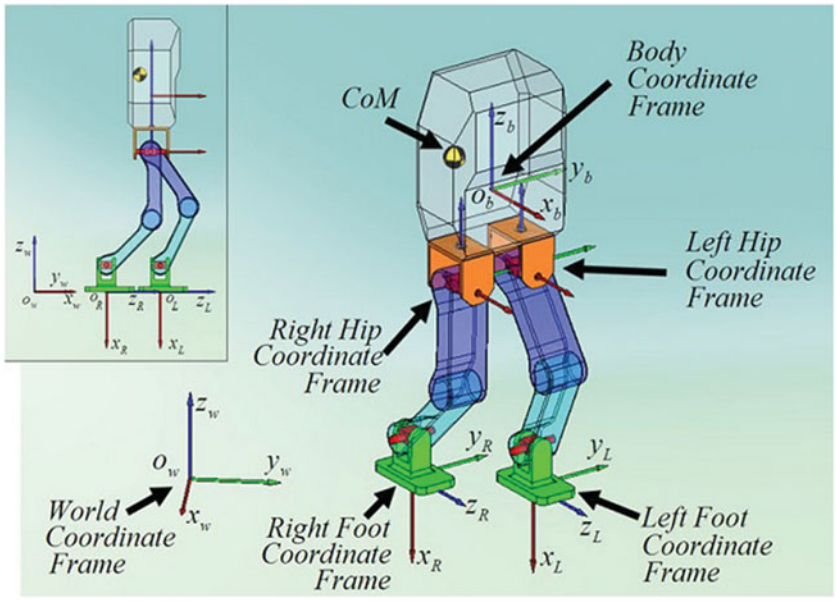

Fig. 4. Coordinate systems. O_w and O_b stand for the origins of the world and body coordinate frames, respectively. The feet coordinate frames are fixed to the feet soles.[37]

R^N, generalized velocities $\mathbf{v}^T = [\mathbf{v}_b^T, \boldsymbol{\omega}_b^T, \boldsymbol{\omega}^T] \in R^3 \times R^3 \times R^N$ and generalized forces $\mathbf{u}^T = [\mathbf{f}_b^T, \mathbf{n}_b^T, \boldsymbol{\tau}^T] \in R^3 \times R^3 \times R^N$, the robot model is

$$\mathbf{H}(\mathbf{x})\dot{\mathbf{v}} + \mathbf{C}(\mathbf{x}, \mathbf{v})\mathbf{v} + \mathbf{g}(\mathbf{x}) + \mathbf{u}_\mathbf{F} = \mathbf{u} + \mathbf{u}_\mathbf{E}, \tag{8}$$

where $\boldsymbol{\theta} \in R^N$ and $\dot{\boldsymbol{\theta}} = \boldsymbol{\omega} \in R^N$ are the joint displacements and angular velocity vectors respectively, $\mathbf{A}_b \in SO(3)$ the transformation matrix giving the position of joint axes relative to the world axes.$\mathbf{p}_b$ and $\dot{\mathbf{p}}_b = \mathbf{v}_b$ the position and linear velocity of the robot base-link coordinate frame center, $\boldsymbol{\omega}_b$ the angular velocity of the robot body coordinate frame and follows the relation $\dot{\mathbf{A}}_b = \boldsymbol{\omega}_b \times \mathbf{A}_b$, $\mathbf{f}_b \in R^3$ and $\mathbf{n}_b \in R^3$ the force and torque vectors generated in the base-link, and $\boldsymbol{\tau}$ the generalized joint control vector. $\mathbf{u}_\mathbf{F}$ the joint frictional forces vector, the matrix H represents the inertia, the $\mathbf{C}(\mathbf{x}, \mathbf{v})$ matrix specifies the centrifugal and coriolis effects and the $\mathbf{g}(\mathbf{x})$ vector specifies the gravity effect. For simplification, the bias term $\mathbf{b}$ is used as $\mathbf{b} = \mathbf{C}(\mathbf{x}, \mathbf{v})\mathbf{v} + \mathbf{g}(\mathbf{x})$. Then, Eq. (8) is rewritten as

$$\mathbf{H}\begin{pmatrix} \dot{\mathbf{v}}_b \\ \dot{\boldsymbol{\omega}}_b \\ \ddot{\boldsymbol{\theta}}_\mathbf{L} \\ \ddot{\boldsymbol{\theta}}_\mathbf{R} \end{pmatrix} + \begin{pmatrix} \mathbf{b_1} \\ \mathbf{b_2} \\ \mathbf{b_L} \\ \mathbf{b_R} \end{pmatrix} + \begin{pmatrix} \mathbf{u}_{\mathbf{F}_1} \\ \mathbf{u}_{\mathbf{F}_2} \\ \mathbf{u}_{\mathbf{F}_\mathbf{L}} \\ \mathbf{u}_{\mathbf{F}_\mathbf{R}} \end{pmatrix} = \begin{pmatrix} \mathbf{f}_b \\ \mathbf{n}_b \\ \boldsymbol{\tau}_\mathbf{L} \\ \boldsymbol{\tau}_\mathbf{R} \end{pmatrix} + \begin{pmatrix} \mathbf{u}_{\mathbf{E}_1} \\ \mathbf{u}_{\mathbf{E}_2} \\ \mathbf{u}_{\mathbf{E}_\mathbf{L}} \\ \mathbf{u}_{\mathbf{E}_\mathbf{R}} \end{pmatrix}, \tag{9}$$

with

$$\mathbf{H} = \begin{pmatrix} H_{11} & H_{12} & H_{13} & H_{14} \\ H_{21} & H_{22} & H_{23} & H_{24} \\ H_{31} & H_{32} & H_{33} & 0 \\ H_{41} & H_{42} & 0 & H_{44} \end{pmatrix},$$

where H_{ij} for $(i, j) \in \{1, 2, 3, 4\}$ are sub-matrices of the robot inertia matrix, $\mathbf{u}_{\mathbf{E}_1}$ the net force effect and $\mathbf{u}_{\mathbf{E}_2}$ the net torque effect of the reaction forces on the base, $\mathbf{u}_{\mathbf{E}_\mathbf{L}}$ and $\mathbf{u}_{\mathbf{E}_\mathbf{R}}$ stand for the effect of reaction forces generated by environmental interaction on the robot joints for the left and right legs respectively. The subscripts $(\,)_\mathbf{L}$ and $(\,)_\mathbf{R}$ stand for the left and right legs respectively.

For force computation, with $\mathbf{f}_b = \mathbf{u}_{\mathbf{F}_1} = 0$, Eq. (9) can be reduced as

$$\mathbf{u}_{\mathbf{E}_1} = \mathbf{H}_F \begin{pmatrix} \dot{\mathbf{v}}_b \\ \dot{\boldsymbol{\omega}}_b \\ \ddot{\boldsymbol{\theta}}_{\mathbf{L}} \\ \ddot{\boldsymbol{\theta}}_{\mathbf{R}} \end{pmatrix} + \mathbf{b}_1, \tag{10}$$

with

$$\mathbf{H}_F = \begin{pmatrix} H_{11} & H_{12} & H_{13} & H_{14} \end{pmatrix}.$$

The computed force vector is related to $\mathbf{u}_{\mathbf{E}_1}$ in Eq. (10) using the Jacobean $\mathbf{J}$ as

$$\mathbf{u}_{\mathbf{E}_1} = \mathbf{J}^{\mathbf{T}} \bar{\mathbf{F}}_{\mathbf{E}}, \tag{11}$$

or in terms of $\bar{\mathbf{F}}_{\mathbf{E}}$

$$\bar{\mathbf{F}}_{\mathbf{E}} = \mathbf{J}(\mathbf{x}) \left(\mathbf{J}^{\mathbf{T}}(\mathbf{x}) \mathbf{J}(\mathbf{x}) \right)^{-1} \mathbf{u}_{\mathbf{E}_1}. \tag{12}$$

The Jacobean $\mathbf{J}$ computation depends on the robot geometry which is known. Substituting Eqs. (11) and (12) into Eq. (10) yields

$$\bar{\mathbf{F}}_{\mathbf{E}} = \mathbf{J}^{\dagger} \left(\mathbf{H}_F \begin{pmatrix} \dot{\mathbf{v}}_b \\ \dot{\boldsymbol{\omega}}_b \\ \ddot{\boldsymbol{\theta}}_{\mathbf{L}} \\ \ddot{\boldsymbol{\theta}}_{\mathbf{R}} \end{pmatrix} + \mathbf{b}_1 \right), \tag{13}$$

with $\mathbf{J}^{\dagger} = \mathbf{J}(\mathbf{x}) \left(\mathbf{J}^{\mathbf{T}}(\mathbf{x}) \mathbf{J}(\mathbf{x}) \right)^{-1}$. Three unknowns exist in Eq. (13), the attitude $\mathbf{A}_b$, the velocity $\mathbf{v}_b$ and the joint angular accelerations. $\mathbf{A}_b$ and $\mathbf{v}_b$ are estimated while the explicit calculation of the joint angular accelerations is avoided as shown later.

4.3.1. Base attitude estimation. The author developed a method that concentrates on the estimation of the attitude from measurements provided by inertial sensors.[38] This method is independent on the robot model so that it can be applied for the humanoids too. In this method, two sequential estimators are used to estimate the attitude. The first one is a Kalman Filter and it is employed for the gravity estimation mainly based on acceleration readings. The second estimator has the structure of an Extended Kalman Filter EKF which uses the gravity estimate generated by the first estimator and rate gyro readings for the orientation estimation. The presented approach uses a quaternion representation. The resulted attitude matrix A_I^w represents the attitude of the IMU frame O_I with respect to the world frame O_w.

It is assumed the IMU is fixed at a known position r and attitude A_I^b with respect to the base frame O_b, thus the base frame attitude $\mathbf{A}_b$ with respect to O_w can be calculated by using A_I^w as

$$\mathbf{A}_b = A_I^w A_b^I. \tag{14}$$

The rotation matrices have the properties $A_b^I = \left(A_I^b\right)^T = \left(A_I^b\right)^{-1}$ since the coordinate system is orthogonal.

4.3.2. Base velocity estimation. The base velocity has an important role in the estimation process. Here a sensor fusion approach is used to estimate the base velocity based on the LIPM.[39] In this model, the base is modeled as a point mass concentrated at the Center of Mass (CoM). The CoM is connected to a stable contact point on the ground using a massless rod which is the idealized model of the supporting leg.[40] The CoM position has fixed height z_c, c_x in the x-direction and c_y in the y-direction. Thus, the CoM position coordinates vector $\mathbf{c}$ in the three dimensional space is $\mathbf{c} = [\, c_x \;\; c_y \;\; z_c \,]^T$. The LIPM relates the CoM states (position, velocity and acceleration) to the feet

contact forces through ZMP $\equiv \mathbf{p_{ZMP}}$. The LIPM is given by

$$\ddot{\mathbf{c}} = \frac{g}{z_c}\left(\mathbf{c} - \mathbf{p_{ZMP}}\right), \tag{15}$$

where g is the constant gravity acceleration and $\ddot{\mathbf{c}}$ the CoM acceleration vector. The model in Eq. (15) requires the $\mathbf{p_{ZMP}}$ and it can be calculated using the feet contact force measurements $\mathbf{F_E}$ to form $\mathbf{p}_{\mathbf{ZMP}}^{\mathbf{F_E}}$ as[41]

$$\mathbf{p}_{\mathbf{ZMP}}^{\mathbf{F_E}} = \frac{\boldsymbol{\rho}_{\mathbf{L}} \sum_{i=1}^{l} {}^{\mathbf{L}}F_N^i + \boldsymbol{\rho}_{\mathbf{R}} \sum_{i=1}^{l} {}^{\mathbf{R}}F_N^i}{\sum_{i=1}^{l} {}^{\mathbf{R}}F_N^i + \sum_{i=1}^{l} {}^{\mathbf{L}}F_N^i}, \tag{16}$$

where

$$\boldsymbol{\rho}_{\mathbf{m}} = \left(\mathbf{p_m} + \mathbf{p_{m,CoP}}\right). \tag{17}$$

Here $\mathbf{p_{m,CoP}}$ is the position of the Center of Pressure CoP for the foot $\mathbf{m}$, and $\mathbf{p_m}$ is the position of the foot frame origin for the leg $\mathbf{m}$ and given by the forward kinematics as $\mathbf{p_m}{=}f_{\mathbf{m}}(\mathbf{x})$.

The considered measurements, inputs and state description determine the state space model of Eq. (15).[11,42,43] Let $\mathrm{x} = \left(\mathbf{c}^T \;\; \dot{\mathbf{c}}^T \;\; \ddot{\mathbf{c}}^T\right)^T$ be the states. Then with this state description, Eq. (15) can be written as Eq. (11)

$$\frac{d}{dt}\begin{bmatrix}\mathbf{c}\\ \dot{\mathbf{c}}\\ \ddot{\mathbf{c}}\end{bmatrix} = \begin{bmatrix}0_3 & I_3 & 0_3\\ 0_3 & 0_3 & I_3\\ 0_3 & 0_3 & 0_3\end{bmatrix}\begin{bmatrix}\mathbf{c}\\ \dot{\mathbf{c}}\\ \ddot{\mathbf{c}}\end{bmatrix} + \begin{bmatrix}0_3\\ 0_3\\ I_3\end{bmatrix}\dddot{\mathbf{c}}, \tag{18}$$

$$\mathbf{p_{ZMP}} = \begin{bmatrix} I_3 & 0_3 & -\frac{z_c}{g}I_3\end{bmatrix}\begin{bmatrix}\mathbf{c}\\ \dot{\mathbf{c}}\\ \ddot{\mathbf{c}}\end{bmatrix}. \tag{19}$$

In discrete form, Eqs. (18) and (19) correspond to

$$\begin{aligned}\begin{bmatrix}\mathbf{c}\\ \dot{\mathbf{c}}\\ \ddot{\mathbf{c}}\end{bmatrix}_k &= \underbrace{\begin{bmatrix} I_3 & I_3T & I_30.5T^2\\ 0_3 & I_3 & I_3T\\ 0_3 & 0_3 & I_3\end{bmatrix}}_{A}\begin{bmatrix}\mathbf{c}\\ \dot{\mathbf{c}}\\ \ddot{\mathbf{c}}\end{bmatrix}_{k-1} + \underbrace{\begin{bmatrix}0_3\\ 0_3\\ TI_3\end{bmatrix}}_{B}\dddot{\mathbf{c}}_k + \mathrm{w}_{k-1}\\ \mathbf{p_{ZMP},}_k &= \underbrace{\begin{bmatrix} I_3 & 0_3 & -\frac{z_c}{g}I_3\end{bmatrix}}_{C}\begin{bmatrix}\mathbf{c}\\ \dot{\mathbf{c}}\\ \ddot{\mathbf{c}}\end{bmatrix}_k + v_k,\end{aligned} \tag{20}$$

with

$$\dddot{\mathbf{c}}_k = \frac{\ddot{\mathbf{c}}_k - \ddot{\mathbf{c}}_{k-1}}{T}. \tag{21}$$

Where k is the time index and $\dot{\mathbf{c}}$ the CoM velocity vector. The input $\dddot{\mathbf{c}}$ is considered to be piecewise constant over the sampling time interval T, i.e. $\dddot{\mathbf{c}}(t) =, \dddot{\mathbf{c}}_{kk},\ t_k \le t < t_{k+1} = t_k + T$. w and v represent the process and measurements noises respectively. They are considered to be Gaussian, independent and mutually uncorrelated with zero mean and covariances Q and R respectively defined as

$$\begin{aligned} &E\left(\mathrm{w}_k\right) = E\left(v_k\right) = E\left(\mathrm{w}_k v_i^T\right) = 0\\ &Q = \delta_{ki}E\left(\mathrm{w}_k \mathrm{w}_i^T\right); R = \delta_{ki}E\left(v_k v_i^T\right)\\ &\delta_{ki} = \begin{Bmatrix}1 & i = k\\ 0 & i \neq k\end{Bmatrix}\end{aligned}, \tag{22}$$

where $E\left(\dot{}\right)$ stands for the expectation of $\left(\dot{}\right)$.

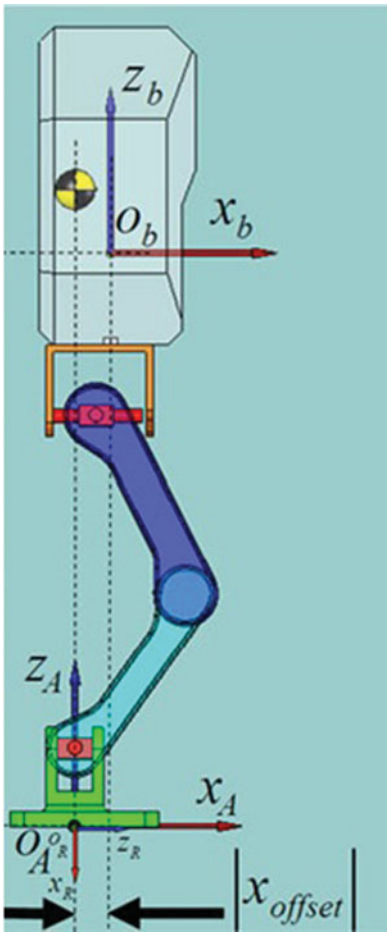

Fig. 5. Body frame offset.

The CoM frame origin is not necessarily to be the same as the body frame. The CoM may have an offset $\mathbf{c}_{\text{offset}}$ as expressed in O_w. An example of this offset is shown in Fig. 5, the CoM has x_{offset} from the body frame which has to be considered in the estimation. The value $\ddot{\mathbf{c}}$ in Eq. (21) is computed by utilizing the IMU acceleration and angular velocity readings $\dot{\mathbf{v}}_I^w$ and $\boldsymbol{\omega}_I^w$ respectively as expressed in O_w. Accordingly, the CoM acceleration is given by

$$\ddot{\mathbf{c}} = \dot{\mathbf{v}}_I^w + \boldsymbol{\omega}_I^w \times \left(\boldsymbol{\omega}_I^w \times (\mathbf{A}_b r + \mathbf{c}_{\text{offset}})\right) + \dot{\boldsymbol{\omega}}_I^w \times (\mathbf{A}_b r + \mathbf{c}_{\text{offset}}), \tag{23}$$

where r is the position of the IMU with respect to O_b.

Then, Eqs. (20), (21) and (23) are used in the adaptive Kalman filter that is proposed by the author.[44] For the given state description, the priori estimate of the state vector $\hat{x}_k^-$ is

$$\hat{x}_k^- = A\hat{x}_{k-1} + Bu_{k-1}. \tag{24}$$

The *a priori* covariance P^- is estimated as

$$P_k^- = AP_{k-1}A^T + Q_{k-1}. \tag{25}$$

The posteriori estimate $\hat{x}$ is

$$\hat{x}_k = \hat{x}_k^- + K_k e_k, \tag{26}$$

where K is Kalman filter gain and e the measurement residual. K and e are defined as

$$K_k = P_k^- C^T \left(C P_k^- C^T + R_k\right)^{-1}, \tag{27}$$

and

$$e_k = \mathbf{p}_{\mathbf{ZMP},k}^{\mathbf{F_E}} - C\hat{x}_k^-, \tag{28}$$

respectively. R is updated as

$$R_k = \left|\text{diag}\left(\alpha_1 R_{k-1} + \Delta R_k\right)\right|, \tag{29}$$

where diag stands for the diagonal matrix and

$$\alpha_1 = \frac{N_R - 1}{N_R}. \tag{30}$$

Here N_R is a positive tuning constant and ΔR is given by

$$\Delta R_k = \frac{1}{N_R - 1}\left(e_k - \bar{e}_k\right)\left(e_k - \bar{e}_k\right)^T - \frac{1}{N_R}\left(C\ P^-\ C^T\right)_k, \tag{31}$$

where $\bar{e}$ is the mean of e and updated as

$$\bar{e}_k = \alpha_1 \bar{e}_{k-1} + \frac{1}{N_R} e_k. \tag{32}$$

Defining I as the identity matrix, then the posteriori covariance P is

$$P_k = \left(I - K_k\ C\right) P_k^-. \tag{33}$$

Defining N_Q as a positive tuning constant, $\hat{\Lambda}$ and $\bar{\Lambda}$ as the state error and its mean respectively, then Q is updated by the expression

$$Q_k = \left|\text{diag}\left(\alpha_2 Q_{k-1} + \Delta Q_k\right)\right|, \tag{34}$$

where

$$\Delta Q_k = \frac{1}{N_Q}\left(P_k - A\ P_{k-1} A^T\right) + \frac{1}{N_Q - 1}\left(\hat{\Lambda}_k - \bar{\Lambda}_k\right)\left(\hat{\Lambda}_k - \bar{\Lambda}_k\right)^T, \tag{35}$$

$$\alpha_2 = \frac{N_Q - 1}{N_Q}, \tag{36}$$

$$\hat{\Lambda}_k = \hat{x}_k - \hat{x}_k^-, \tag{37}$$

and

$$\bar{\Lambda}_k = \alpha_2 \bar{\Lambda}_{k-1} + \frac{1}{N_Q}\hat{\Lambda}_k. \tag{38}$$

N_Q and N_R are tuning parameters and their values are user defined based on the system noise characteristics. For big values of N_Q and N_R (for example > 1000), the AKF is close to Kalman filter. Basically, for a noisy system, N_Q and N_R are selected to be big for smooth estimates, however, for less noisy systems, they are selected to be small but not less than 50.[44] The initial values of $\bar{e}_0$ and $\bar{\Lambda}_0$ are zeros. The values of Q and R are crucial for Kalman filter estimation, the estimated state $\hat{x}_k$ will be biased if the value of Q is too small with respect to the correct value, and $\hat{x}_k$ will oscillate

around the true value if the value of Q is too large with respect to the correct value. This problem is solved in this AKF, since the values of Q and R are updated in each cycle and, therefore, several initializations work.

For convenience, the time index k is dropped later on. Then, the estimated states are used to calculate the base frame position and velocity states as

$$\mathbf{p}_b = \hat{\mathbf{c}} + \mathbf{c}_{\text{offset}}, \tag{39}$$

and

$$\mathbf{v}_b = \dot{\hat{\mathbf{c}}} + \boldsymbol{\omega}_b^w \times \mathbf{c}_{\text{offset}}, \tag{40}$$

respectively.

4.3.3. Joint angular accelerations calculation avoidance. The explicit calculation of the angular accelerations is avoided using the filtered dynamic model method.[45] This is accomplished by filtering both sides of Eq. (13) using a proper stable filter. A first order filter transfer function Z is considered with the constants K_F and λ as

$$Z(s) = K_F \frac{1}{s+\lambda}, \tag{41}$$

its impulse response is

$$z(t) = \ell^{-1}(Z(s)) = K_F e^{-\lambda t}, \tag{42}$$

where $\ell^{-1}(.)$ is the inverse Laplace transform. Equation (13) is composed of $3 \times 2 \times l$ equations, each of them is filtered by Eq. (41). Therefore, there will be $3 \times 2 \times l$ filters with impulse responses which can be organized into a matrix as

$$\mathbf{z}(t) = \begin{bmatrix} K_{F,_1} e^{-\lambda_1 t} & & 0 \\ & \ddots & \\ 0 & & K_{F,(3\times 2\times l)} e^{-\lambda_{3\times 2\times l} t} \end{bmatrix}_{(3\times 2\times l)\times(3\times 2\times l)}, \tag{43}$$

where $K_{F,i}$ and λ_i for $i = 1, 2, \ldots, 3 \times 2 \times l$ are the i^{th} equation filter constants. The multiplication in the frequency domain is equivalent to the convolution in time domain, thus the filtered version of Eq. (13) can be obtained as

$$\begin{aligned} \int_0^t \mathbf{z}(t-\tau)\bar{\mathbf{F}}_{\mathbf{E}} d\tau = & \int_0^t \mathbf{z}(t-\tau)\mathbf{J}^{\dagger}(H_{13} \quad H_{14}) \begin{pmatrix} \ddot{\boldsymbol{\theta}}_{\mathbf{L}} \\ \ddot{\boldsymbol{\theta}}_{\mathbf{R}} \end{pmatrix} d\tau \\ & + \int_0^t \mathbf{z}(t-\tau)\mathbf{J}^{\dagger} \left((H_{11} \quad H_{12}) \begin{pmatrix} \dot{\mathbf{v}}_b \\ \dot{\boldsymbol{\omega}}_b \end{pmatrix} + \mathbf{b}_1 \right) d\tau, \end{aligned} \tag{44}$$

where τ is the integration variable and all time dependent quantities are temporarily considered to depend on τ instead of t. For simplification, the term $\xi = \mathbf{J}^{\dagger}\begin{pmatrix} H_{13} & H_{14} \end{pmatrix}$ is introduced. Then, the term $\int_0^t \mathbf{z}(t-\tau)\xi(\begin{matrix} \ddot{\boldsymbol{\theta}}_{\mathbf{L}} \\ \ddot{\boldsymbol{\theta}}_{\mathbf{R}} \end{matrix})d\tau$ can be integrated by parts with $\dot{\boldsymbol{\theta}}_{\mathbf{L}}(0) = \dot{\boldsymbol{\theta}}_{\mathbf{R}}(0) = 0$ and $\mathbf{z}(0) = \mathbf{K}_F = [\begin{matrix} K_{F,_1} & & 0 \\ & \ddots & \\ 0 & & K_{F,3\times 2\times l} \end{matrix}]$ as

$$\int_0^t \mathbf{z}(t-\tau)\xi \begin{pmatrix} \ddot{\boldsymbol{\theta}}_{\mathbf{L}} \\ \ddot{\boldsymbol{\theta}}_{\mathbf{R}} \end{pmatrix} d\tau = \mathbf{K}_F \xi \begin{pmatrix} \dot{\boldsymbol{\theta}}_{\mathbf{L}} \\ \dot{\boldsymbol{\theta}}_{\mathbf{R}} \end{pmatrix} - \int_0^t \mathbf{z}(t-\tau)\dot{\xi} \begin{pmatrix} \dot{\boldsymbol{\theta}}_{\mathbf{L}} \\ \dot{\boldsymbol{\theta}}_{\mathbf{R}} \end{pmatrix} d\tau - \int_0^t \dot{\mathbf{z}}(t-\tau)\xi \begin{pmatrix} \dot{\boldsymbol{\theta}}_{\mathbf{L}} \\ \dot{\boldsymbol{\theta}}_{\mathbf{R}} \end{pmatrix} d\tau, \tag{45}$$

where

$$\dot{\xi} = \mathbf{J}^{\dagger}\begin{pmatrix}\dot{H}_{13} & \dot{H}_{14}\end{pmatrix} + \dot{\mathbf{J}}^{\dagger}\begin{pmatrix}H_{13} & H_{14}\end{pmatrix}. \tag{46}$$

Then, the filtered version of the force is

$$\int_0^t \mathbf{z}(t-\tau)\bar{\mathbf{F}}_{\mathbf{E}}d\tau = \mathbf{K}_F\xi\begin{pmatrix}\dot{\boldsymbol{\theta}}_{\mathbf{L}}\\ \dot{\boldsymbol{\theta}}_{\mathbf{R}}\end{pmatrix} - \int_0^t \mathbf{z}(t-\tau)\dot{\xi}\begin{pmatrix}\dot{\boldsymbol{\theta}}_{\mathbf{L}}\\ \dot{\boldsymbol{\theta}}_{\mathbf{R}}\end{pmatrix}d\tau$$
$$+ \int_0^t \mathbf{z}(t-\tau)\mathbf{J}^{\dagger}\left(\begin{pmatrix}H_{11} & H_{12}\end{pmatrix}\begin{pmatrix}\dot{\mathbf{v}}_b\\ \dot{\boldsymbol{\omega}}_b\end{pmatrix} + \mathbf{b}_1\right)d\tau - \int_0^t \dot{\mathbf{z}}(t-\tau)\xi\begin{pmatrix}\dot{\boldsymbol{\theta}}_{\mathbf{L}}\\ \dot{\boldsymbol{\theta}}_{\mathbf{R}}\end{pmatrix}d\tau. \tag{47}$$

All the terms are filtered using Eq. (41) except $\int_0^t \dot{\mathbf{z}}(t-\tau)\xi(\begin{smallmatrix}\dot{\boldsymbol{\theta}}_{\mathbf{L}}\\ \dot{\boldsymbol{\theta}}_{\mathbf{R}}\end{smallmatrix})d\tau$. It is filtered by

$$Z_2(s) = \ell\{\dot{z}(t)\} = \ell\left\{-K_F\lambda e^{-\lambda t}\right\} = -K_F\frac{\lambda}{s+\lambda}, \tag{48}$$

or in matrix form

$$\mathbf{z}_2(t) = -\begin{bmatrix}K_{F,_1}\lambda_1 e^{-\lambda_1 t} & & 0\\ & \ddots & \\ 0 & & K_{F,3\times2\times l}\lambda_{3\times2\times l}e^{-\lambda_{3\times2\times l}t}\end{bmatrix}_{(3\times2\times l)\times(3\times2\times l)}. \tag{49}$$

To write Eq. (47) in more proper form, the notation $\langle\chi\rangle_{\beta}$ is introduced. This notation indicates that the term χ is filtered using the filter β. Accordingly, Eq. (47) is written as

$$\langle\bar{\mathbf{F}}_{\mathbf{E}}\rangle_{Z(s)} = \mathbf{K}_F\xi\begin{pmatrix}\dot{\boldsymbol{\theta}}_{\mathbf{L}}\\ \dot{\boldsymbol{\theta}}_{\mathbf{R}}\end{pmatrix} - \left\langle\dot{\xi}\begin{pmatrix}\dot{\boldsymbol{\theta}}_{\mathbf{L}}\\ \dot{\boldsymbol{\theta}}_{\mathbf{R}}\end{pmatrix}\right\rangle_{Z(s)}$$
$$+ \left\langle\mathbf{J}^{\dagger}\left(\begin{pmatrix}H_{11} & H_{12}\end{pmatrix}\begin{pmatrix}\dot{\mathbf{v}}_b\\ \dot{\boldsymbol{\omega}}_b\end{pmatrix} + \mathbf{b}_1\right)\right\rangle_{Z(s)} - \left\langle\xi\begin{pmatrix}\dot{\boldsymbol{\theta}}_{\mathbf{L}}\\ \dot{\boldsymbol{\theta}}_{\mathbf{R}}\end{pmatrix}\right\rangle_{Z_2(s)}. \tag{50}$$

From the estimated filtered forces vector $\langle\bar{\mathbf{F}}_{\mathbf{E}}\rangle_{Z_F(s)}$, the filtered components are obtained from the vector $\langle\bar{\mathbf{F}}_{\mathbf{E}}\rangle_{Z_F(s)} \equiv \langle[\,\bar{\mathbf{F}}^T_{\mathbf{E_R}}\ \bar{\mathbf{F}}^T_{\mathbf{E_L}}\,]^T\rangle_{Z_F(s)}$ and they are ordered as in Eq. (6). Then out of these forces, the tangential components are used for the slip detection as in Eq. (3).

The gain and the cut-off frequency of the first order filter affect the results. Their values depend on the highest meaningful frequency in the measurements ($\mathbf{F}_{\mathbf{E}}$ and $\dot{\mathbf{v}}_b$). The cut-off frequency value should be higher than the highest meaningful frequency, at the same time it should be able to smooth the measurements and reject the other higher frequencies. Therefore, the cut-off frequency value must not be too high. The gain of the filter can be chosen as $K_F = \lambda$ and thus the gain of the first order filter in the low frequency region is unity and at the cut-off frequency is 0.707.

However, the acceleration and force reading along with Eqs. (4) and (3) can be used to detect the slip only. They cannot be used alone to predict the slip due to the friction behavior. To overcome this challenge, a slip prediction approach is introduced.

5. Slip Prediction

Slip prediction is based on the friction behavior at the low speed. The design for both x- and y-directions is the same. Therefore, for convenience the subscripts x and y are deleted. For the nonslipping case, F_t must be in the static friction area where $F_t < F_s$. Equivalently, the allowable force F_t such that the object is not slipping must be inside the cone Fig. 1c.

However, F_s (or μ_{static}) changes according to the surfaces. Thus, specifying a value for F_s limits the motion to one surface or limited surfaces. One more challenge comes from the friction behavior. Precisely, it is due to that the kinetic friction is less than the static friction. This necessitates looking

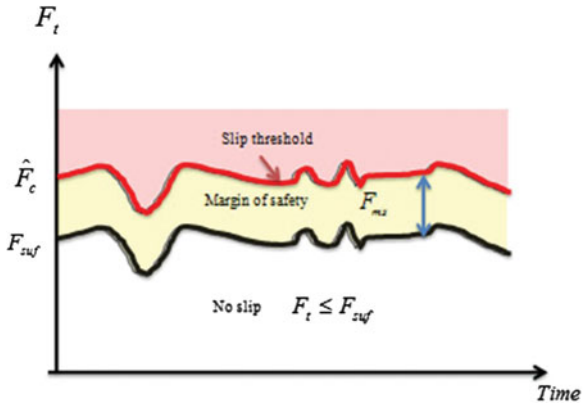

Fig. 6. Slip prediction regions.

at the friction behavior in Fig. 2. Since the interest is in the slip prediction at low speed, F_v is out of scope. According to the friction behavior, the minimum friction force beyond which slip will be observed is F_c. This force is used instead of F_s and thus overcome the aforementioned challenge. To cope with several surfaces, F_c is estimated online in an adaptive way. Hence, the walking will not be limited to certain surfaces.

5.1. Slip prediction approach

The slip prediction approach for both feet is the same. It is based on the estimated value $\hat{F}_c$ (or $\hat{\mu}_c$) as a slip threshold. A safety margin with a value F_{ms} is introduced to design the slip predictor. Also, the proposed method defines a sufficient friction force F_{suf} such that $F_{\text{suf}} + F_{ms} \leq \hat{F}_c$. Accordingly, the foot never slips if the inequality $F_t \leq F_{\text{suf}}$ is satisfied as in Fig. 6. The given safety margin leads to the simple slip prediction scheme: At each time instant k, if $\mathbf{F}_{\text{slip}} = 0$ or $\ddot{\mathbf{p}} \leq Tr$, then the object will not slip if $F_t \leq F_{\text{suf}}$ or tends to slip if $F_t \in \left(F_{\text{suf}}, \hat{F}_c = F_{\text{suf}} + F_{ms}\right)$, i.e.

$$\text{if} \begin{cases} F_{\text{suf}}(k) < F_t(k) < \hat{F}_c(k) & \text{tends to slip} \\ F_t(k) \leq F_{\text{suf}}(k) & \text{no slipping} \end{cases}, \tag{51}$$

however, $\hat{F}_c$ still unknown. It is estimated online as in the next section.

5.2. Slip threshold estimation

The threshold F_c estimation follows whether the foot is slipping or not based on Eq. (4) or $\ddot{\mathbf{p}} \leq Tr$. For the parameter estimation, $\hat{F}_c$ and $\hat{F}_s$ are defined as the estimated variables. The estimation is done empirically without using models in the following steps:

Step 1: Initialize F_s, F_{st}, F_{ms} and $\hat{F}_c$.

Step 2: Check whether the foot is in contact with the floor or not. If it is in contact go to step 3, else the variables are

$$\begin{aligned} \hat{F}_c(k) &= \hat{F}_c(k-1) \\ \hat{F}_s(k) &= \hat{F}_s(k-1) \\ \hat{F}_{st}(k) &= \hat{F}_{st}(k-1). \end{aligned} \tag{52}$$

Step 3: Check whether the foot is slipping or not.

Step 4: if it is not slipping, then the friction force is the same as the measured tangential force as in

$$F_f(k) = F_t(k), \tag{53}$$

and the estimated static friction $\hat{F}_s$ is the maximum value of the friction and obtained by

$$\hat{F}_s(k) = \max\left(\left|F_f(k)\right|, \left|\hat{F}_s(k-1)\right|\right). \tag{54}$$

Bearing in mind $\hat{F}_c(k-1)$, the coulomb friction $\hat{F}_c$ is estimated as

$$\hat{F}_c(k) = \min\left(\hat{F}_s(k), \hat{F}_c(k-1)\right). \tag{55}$$

However, the friction force may exceed the threshold, i.e. $\left|F_f(k)\right| > \hat{F}_c(k) + \hat{F}_{st}(k-1)$, for this case, the coulomb friction is calculated again as

$$\hat{F}_c(k) = \left|\left|F_f(k)\right| - \hat{F}_{st}(k-1)\right|. \tag{56}$$

The sufficient friction F_{suf} is calculated as

$$\begin{array}{c} F_{\text{suf}}(k) = \hat{F}_c(k) - F_{ms} \\ F_{\text{suf}}(k) \geq 0 \end{array}, \tag{57}$$

Step 5: if the foot is slipping, then calculate $\hat{F}_c$ as

$$\hat{F}_c(k) = \min\left(\left|F_f(k)\right|, \left|\hat{F}_c(k-1)\right|\right) \tag{58}$$

$\hat{F}_s$, $\hat{F}_{st}$ and F_{suf} are obtained by

$$\hat{F}_s(k) = \hat{F}_s(k-1) \tag{59}$$

$$\begin{array}{c} \hat{F}_{st}(k) = \hat{F}_s(k-1) - \hat{F}_c, \\ \hat{F}_{st} \geq 0 \end{array} \tag{60}$$

and

$$\begin{array}{c} F_{\text{suf}}(k) = \hat{F}_c(k) - F_{ms} \\ F_{\text{suf}}(k) \geq 0 \end{array}, \tag{61}$$

respectively.

Step 6: update the variables

$$\begin{aligned} \hat{F}_c(k-1) &= \hat{F}_c(k) \\ \hat{F}_s(k-1) &= \hat{F}_s(k) \\ \hat{F}_{st}(k-1) &= \hat{F}_{st}(k). \end{aligned} \tag{62}$$

Step 7: go to step 2.

6. Experimental Results

The proposed method is tested here on the bipedal humanoid robot SURALP (Fig. 8).[46] The dimensional drawings are in Fig. 8. The robot weight and length parameters are listed in Table I. The robot actuation system is composed of DC motors, belt-bully system and Harmonic Drive Reduction Gears (HDRG). The belt-bully system transmits the motor rotation to the HDRG. The motors include encoders to measure the motor angular position. SURALP is equipped with six-axes force/torque sensors assembled at the ankles and a rate gyro and an accelerometer which are positioned at the robot torso. Also, SURALP is equipped with a three-axes accelerometer fixed at the foot. Therefore, the experiments depend on case one according to the available measurements. The foot is checked

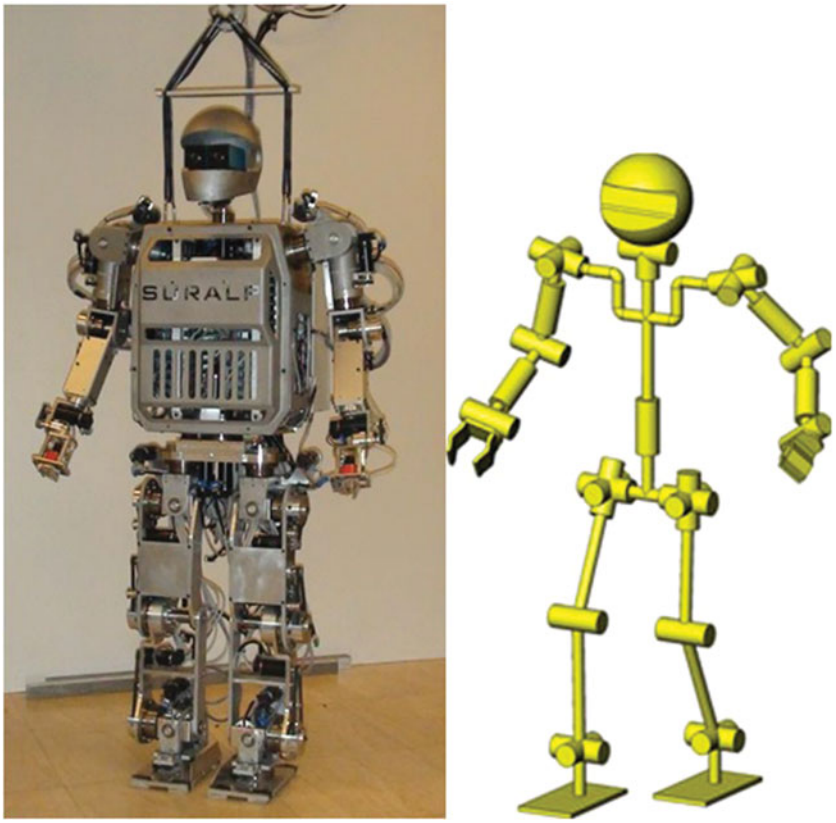

Fig. 7. SURALP, kinematic arrangement.

Table I. Length parameters of the robot.

Parameter	Value
Upper leg length	280 mm
Lower leg length	270 mm
Sole-ankle distance	124 mm
Foot dimensions	240 mm × 150 mm
Upper arm length	219 mm
Lower arm length	255 mm
Robot weight	114 kg

whether it is in contact with the ground or not using the measured normal force from the force/torque sensor.

As an implementation consideration, the accelerometer gives a reading even though the biped is not moving. Therefore, the slip is detected if the acceleration readings are larger than a threshold Tr i.e. $\ddot{\mathbf{p}} \geq Tr$. This threshold depends on the initial accelerometer reading and the required confidence.

The measured acceleration and force are used first to detect whether there is slipping or not. If there is no slipping, they are used to predict the slip occurrence. To accomplish this, first the friction terms are estimated and then used for the slip prediction procedure.

6.1. Estimated friction terms

The estimated friction terms for the right foot in the x-direction are shown in Fig. 9. This estimation is based on the experimentally observed $Tr = 0.09$ and follows the Eqs. (52)–(62). The repeated peaks pattern of the acceleration represents the leg when it is swinging. The algorithm detects whether the foot is in contact or not and updates the variables accordingly. When the leg is swinging, the variables values are calculated as in Eq. (52). The estimated $\hat{F}_s$ and $\hat{F}_{st}$ are shown in Fig. 9c. $\hat{F}_c$ and F_{suf}

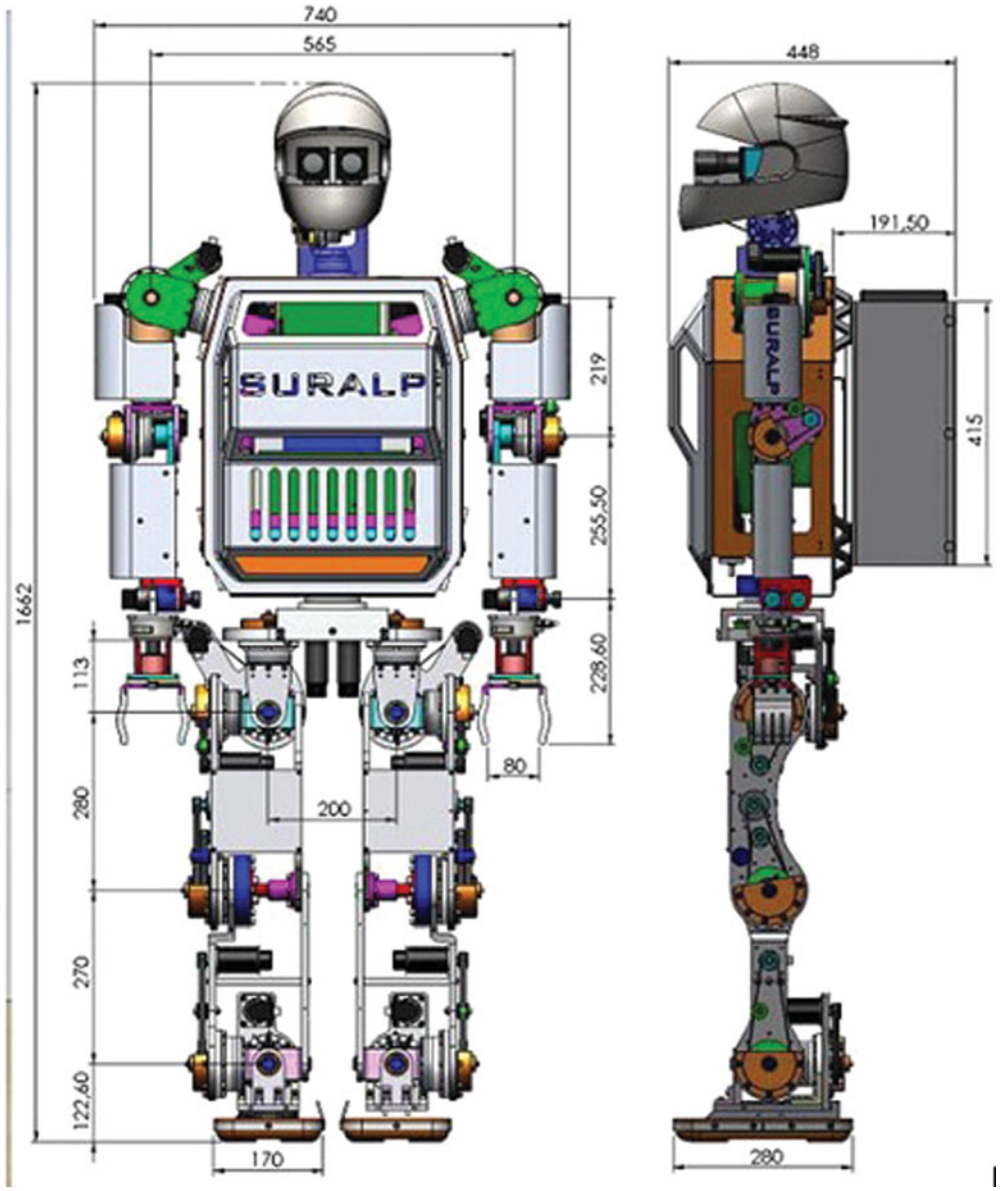

Fig. 8. SURALP dimensional drawings.

are presented in Fig. 9d. From the Figure, the estimated friction terms are observed as: $\hat{F}_s = 85N$, $\hat{F}_c = 21N$, $F_{\text{suf}} = \hat{F}_c - 5 = 16N$, $F_{ms} = 5N$, and $\hat{F}_{st} = 64N$.

6.2. Slip prediction performance

The estimated friction terms are used for slip prediction. The test is carried on a new walk of SURALP, hence on new data. The real slipping occurrence is detected based on the accelerometer reading with $Tr = 0.09$ as in Fig. 10b. This accelerometer is attached to the foot. The estimated and predicted slip are based on the proposed algorithm. In other words, when $|F_t| \geq \left|\hat{F}_c\right|$ then the foot is slipping, when $\left|\hat{F}_{\text{suf}}\right| \leq |F_t| < \left|\hat{F}_c\right|$ then the foot tends to slip, and when $|F_t| < \left|\hat{F}_{\text{suf}}\right|$ then the foot will not slip as shown in Fig. 10a.

While walking, the biped switches its legs from the double support phase DS to the single support phase SS and so forth. The SS phase is either left single support LS phase or right single support RS phase. At each step the biped walks, the controller stabilizes the robot based on the force/torque sensor to achieve the ZMP criterion. This explains the variations in the measured tangential force all

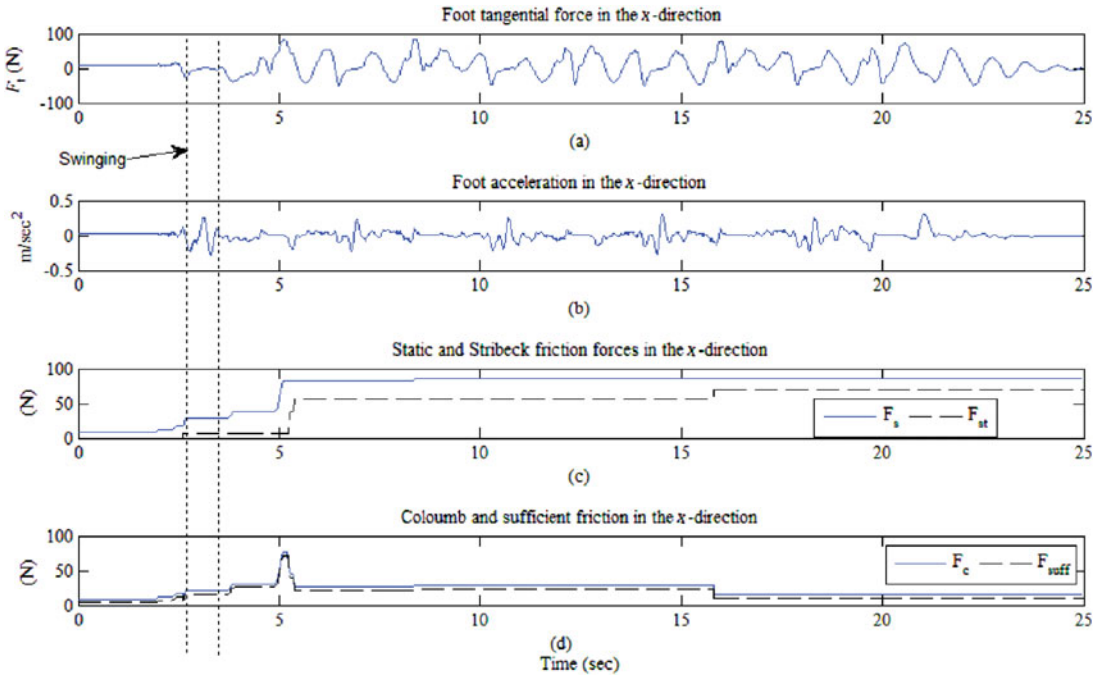

Fig. 9. Friction parameters update in the x-direction.

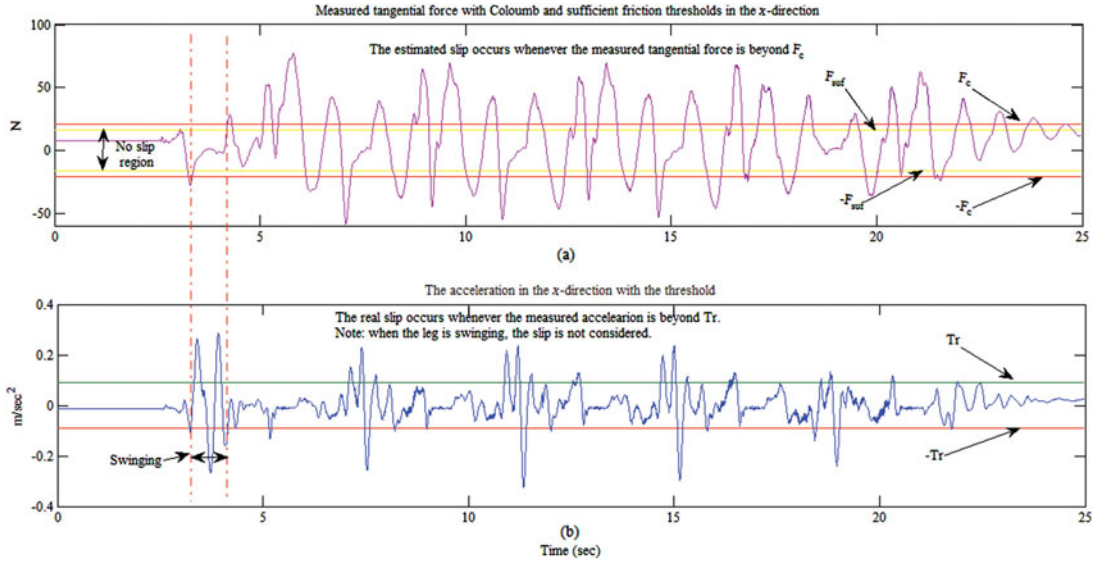

Fig. 10. Slip prediction test in the x-direction.

the time as in Fig. 10a. These variations in the tangential force affect the prediction performance by giving false slipping alarms or false alarms of slipping tendency.

The estimated slip occurs whenever the measured tangential force is beyond $\hat{F}_c$ as in Fig. 10a. This relationship can be explained as follows: for the nonslipping case, the applied tangential forces are equal to the friction forces between the foot and the contact surface in the static region as shown in Fig. 2. On the other hand, the slip occurs when the applied tangential forces are larger than the friction forces. According to the friction behavior in Fig. 2, and since F_v is out of scope at low speed, the minimum friction force beyond which slip will be observed is F_c. Therefore, if the condition $F_t < \hat{F}_c$ is satisfied then F_t is in the static region, otherwise the slip occurs.

While walking, the real slip occurrence of the biped is detected by the accelerometer readings as shown in Fig. 10b. Examples of slipping occurrence are shown in Fig. 11b (zoomed version of

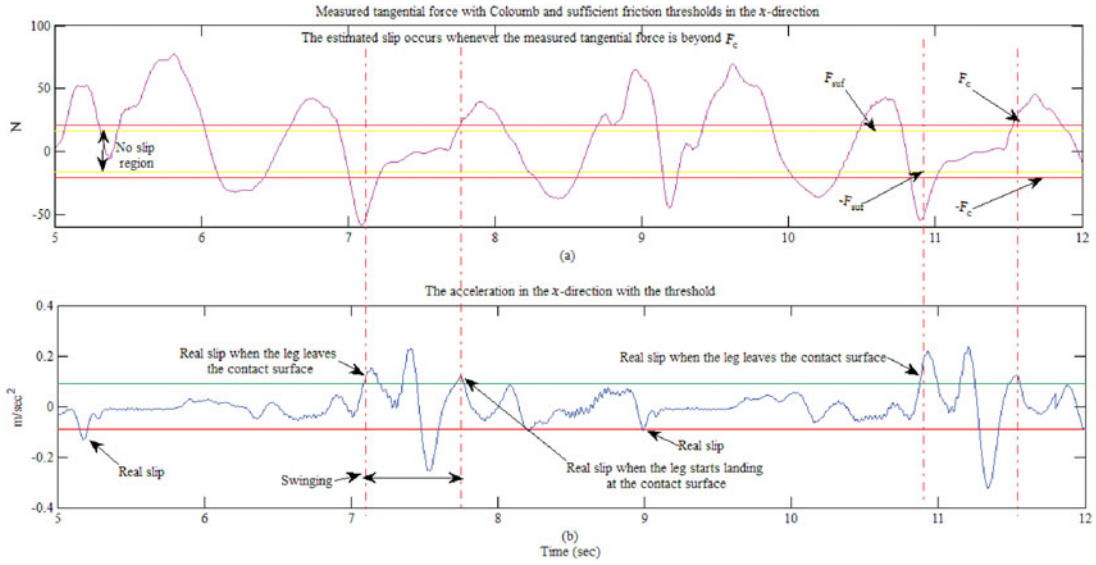

Fig. 11. Zoomed version of Fig. 10 with slipping occurrence examples.

Fig. 10). The biped does not slip whenever the accelerometer reading is between the threshold lines. However, whenever the measured acceleration is beyond Tr the real slip occurs. As in Fig. 11b, the slip occurs when the right foot starts leaving the ground so that the biped switches from DS to LS and when the right foot starts landing so that the biped switches from LS to DS. Further, the slip occurs at other times of walking such as at the time instant t = 5.2 sec and t = 9 sec. The proposed approach detected the slipping occurrences as shown in Fig. 10a and Fig. 11a. Furthermore, the algorithm predicted the slip occurrence due to the design approach, since the tangential forces passed beyond F_{suf} and entered the margin of safety before the slip occurrence.

One challenge to this approach is the false slipping alarms, an example of these alarms is the one shown in Fig. 11a between the time t = 5.5 sec and t = 6 sec. Although there is no real slipping based on the accelerometer reading for the same period in Fig. 11b, the proposed approach detected a false slip occurrence. These false alarms are due to two reasons: the first reason is that the tangential force value may exceed the estimated coulomb friction value and the foot is still not slipping. In this case, the tangential force is in the static region $F_c < F_t < F_s$ as shown in Fig. 2. The second reason depends on the control approach of the biped. For SURALP, at each step the biped walks, the controller stabilizes the robot based on the force/torque sensor to achieve the ZMP criterion, thus F_t varies all the time. These false slipping alarms can be reduced by changing the thresholds. However, this may lead to false nonslipping deductions.

This work assumes that there will be a controller to prevent slipping and compensate for the slip occurrence. The controller has a null function in the nonslipping region. However, its function is to prevent the biped from slipping in case of predicted slip tendency or to compensate for the slip. The controller utilization percentage depends on the proposed algorithm and hence on the thresholds. For this experiment, and according to Fig. 10, the controller utilization is approximately 54%.

7. Conclusion

A novel measurement-based method for online friction estimation is proposed. Based on the friction behavior, the coulomb, Stribeck and static friction terms between the foot sole and the contact surface are estimated adaptively. The estimation is based on acceleration and force measurements. The coulomb friction is used as a threshold for slip detection. To predict the slip occurrence, a margin of safety with coulomb friction is considered. Whenever the measured force enters this margin, then the foot is going to slip. The experimental results demonstrate the proposed method. The accuracy of the algorithm depends on the selected thresholds. Further, while low acceleration thresholds increase the false slipping alarms, high acceleration thresholds increase the false nonslipping alarms.

References

1. K. Erbatur and O. Kurt, "Natural ZMP trajectories for biped robot reference generation," *IEEE Trans. Ind. Electron.* **56**, 835–845 (Mar. 2009).
2. M. Vukobratovi'C and B. Borovac, "Zero-moment point - thirty five years of its life," *Int. J. Humanoid Robot. (IJHR)* **01**, 157–173 (2004).
3. H. Hirukawa, S. Hattori, K. Harada, S. Kajita, K. Kaneko, F. Kanehiro, K. Fujiwara and M. Morisawa, "A Universal Stability Criterion of the Foot Contact of Legged Robots - Adios ZMP," *Proceedings of the IEEE International Conference on Robotics and Automation*, Orlando, FL (2006) pp. 1976–1983.
4. B. J. Stephens and C. G. Atkeson, "Dynamic Balance Force Control for Compliant Humanoid Robots," *Proceedings of the IEEE/RSJ International Conference on Intelligent Robots and Systems (IROS)*, Taipei (2010) pp. 1248–1255.
5. C. Zhu and A. Kawamura, "What is the Real Frictional Constraint in Biped Walking?-Discussion on Frictional Slip with Rotation," *IEEE/RSJ International Conference on*, *Intelligent Robots and Systems*, Beijing (2006) pp. 5762–5768.
6. B. Stephens and C. Atkeson, "Modeling and Control of Periodic Humanoid Balance using the Linear Biped Model," *IEEE-RAS International Conference on Humanoid Robots*, Paris (2009) pp. 379–384.
7. C. Yang and Q. Wu, "Effects of Gravity and Friction Constraints on Bipedal Balance Control," *Proceedings of 2005 IEEE Conference on*, *Control Applications, CCA 2005*, Toronto, Ont (2005) pp. 1093–1098.
8. G. Kinoshita, T. Kimura and M. Shimojo, "Dynamic Sensing Experiments of Reaction Force Distributions on the Sole of a Walking Humanoid Robot," *Proceedings of International Conference on Intelligent Robots and Systems*, (2003) pp. 1413–1418.
9. K. Nishiwaki, Y. Murakami, S. Kagami, Y. Kuniyoshi, M. Inaba and H. Inoue, "A Six-Axis Force Sensor with Parallel Support Mechanism to Measure the Ground Reaction Force of Humanoid Robot," *Proceedings of IEEE International Conference on Robotics and Automation*, Washington, DC (2002) pp. 2277–2282.
10. L. Sentis and O. Khatib, "A Whole-Body Control Framework for Humanoids Operating in Human Environments," *Proceedings 2006 IEEE International Conference on*, *Robotics and Automation, ICRA 2006*, Orlando, FL (2006) pp. 2641–2648.
11. S. Kajita, F. Kanehiro, K. Kaneko, K. Fujiwara, K. Harada, K. Yokoi and H. Hirukawa, "Biped Walking Pattern Generation by using Preview Control of Zero-Moment Point," *Proceedings of IEEE International Conference on Robotics and Automation ICRA* (2003), vol. 2, pp. 1620–1626.
12. B. Ugurlu, J. A. Saglia, N. G. Tsagarakis, S. Morfey and D. G. Caldwell, "Bipedal hopping pattern generation for passively compliant humanoids: Exploiting the resonance," *IEEE Trans. Ind. Electron.* **61**, 5431–5443 (2014).
13. B. Ugurlu, J. A. Saglia, N. G. Tsagarakis and D. G. Caldwell, "Hopping at the Resonance Frequency: A Trajectory Generation Technique for Bipedal Robots with Elastic Joints," *IEEE International Conference on*, *Robotics and Automation (ICRA)*, Saint Paul, MN (2012) pp. 1436–1443.
14. P. B. Wieber, "Viability and Predictive Control for Safe Locomotion," *IEEE/RSJ International Conference on*, *Intelligent Robots and Systems, IROS 2008*, Nice (2008) pp. 1103–1108.
15. S. Kajita, K. Kaneko, K. Harada, F. Kanehiro, K. Fujiwara and H. Hirukawa, "Biped Walking on a Low Friction Floor," *IEEE/RSJ International Conference on*, *Intelligent Robots and Systems, (IROS 2004)*, (2004) pp. 3546–3552.
16. C. A. Klein and S. Kittivatcharapong, "Optimal force distribution for the legs of a walking machine with friction cone constraints," *IEEE Trans. Robot. Autom.* **6**, 73–85 (1990).
17. P. Jong Hyeon and K. Ohung, "Reflex Control of Biped Robot Locomotion on a Slippery Surface," *Proceedings 2001 ICRA. IEEE International Conference on*, *Robotics and Automation*, (2001) pp. 4134–4139.
18. G. Boone and J. Hodgins, "Slipping and tripping reflexes for bipedal robots," *Auton. Robots*, **4**, 259–271 (Jan. 9, 1997).
19. H. Yamamoto and K. Ohnishi, "An Approach to Stable Walking on Unknown Slippery Floor for Biped Robot," *The 27th Annual Conference of the IEEE*, *Industrial Electronics Society, IECON '01*, Denver, CO (2001) pp. 1728–1733.
20. K. Kaneko, F. Kanehiro, S. Kajita, M. Morisawa, K. Fujiwara, K. Harada and H. Hirukawa, "Slip Observer for Walking on a Low Friction Floor," *IEEE/RSJ International Conference on*, *Intelligent Robots and Systems, 2005. (IROS 2005)*, (2005) pp. 634–640.
21. H. Takemura, M. Deguchi, J. Ueda, Y. Matsumoto and T. Ogasawara, "Slip-adaptive walk of quadruped robot," *Robot. Auton. Syst.* **53**, 124–141 (Nov. 30, 2005).
22. H. Onodera, T. Yamaguchi, H. Yamanouchi, K. Nagamori, M. Yano, Y. Hirata and K. Hokkirigawa, "Analysis of the Slip-Related Falls and Fall Prevention with an Intelligent Shoe System," *3rd IEEE RAS and EMBS International Conference on*, *Biomedical Robotics and Biomechatronics (BioRob)*, Tokyo (2010) pp. 616–620.
23. L. S. Lincoln and S. J. M. Bamberg, "Insole Sensor System for Real-Time Detection of Biped Slip," *Annual International Conference of the IEEE*, *Engineering in Medicine and Biology Society (EMBC)*, Buenos Aires (2010) pp. 1449–1452.
24. F. Cordes, S. Bartsch, T. Birnschein, D. Kuehn and F. Kirchner, "Towards an Intelligent Foot for Walking and Climbing Robots," *41st International Symposium on and 2010 6th German Conference on Robotics (ROBOTIK)*, *Robotics (ISR)*, Munich, Germany (2010) pp. 1–8.

25. N. Okita and H. Sommer, "A Novel Foot Slip Detection Algorithm using Unscented Kalman Filter Innovation," *American Control Conference (ACC)*, Montreal, QC (2012) pp. 5163–5168.
26. I. Hashlamon and K. Erbatur, "Simple Virtual Slip Force Sensor for walking Biped Robots," *9th Asian, Control Conference (ASCC)*, Istanbul (2013) pp. 1–5.
27. S. Roosen, "Ground-Contact Friction Estimation and Slip Prevention in Bipedal Robots," *Mechanical Engineering*. vol. (Master: University of Melbourne, 2012).
28. C. J. Tsaprounis and N. A. Aspragathos, "A linear differential formulation of friction forces for adaptive estimator algorithms," *Robotica,* **19**, 407–421 (2001).
29. P. Dahl, "A solid friction model," DTIC Document 1968.
30. B. Armstrong-Hélouvry, P. Dupont and C. C. De Wit, "A survey of models, analysis tools and compensation methods for the control of machines with friction," *Automatica,* **30**, 1083–1138 (1994).
31. C. C. de Wit, H. Olsson, K. J. Astrom and P. Lischinsky, "A new model for control of systems with friction," *IEEE Trans. Autom. Control*, **40**, 419–425 (1995).
32. J. Swevers, F. Al-Bender, C. G. Ganseman and T. Projogo, "An integrated friction model structure with improved presliding behavior for accurate friction compensation," *IEEE Trans. Autom. Control*, **45**, 675–686 (2000).
33. R. H. A. Hellsen, G. Z. Angelis, M. J. G. van de Molengraft, A. G. de Jager and J. J. Kok, "Grey-box modeling of friction: An experimental case-study," *Eur. J. Control*, **6**, 258–267 (2000).
34. V. Lampaert, J. Swevers and F. Al-Bender, "Modification of the Leuven integrated friction model structure," *IEEE Trans. Autom. Control*, **47**, 683–687 (2002).
35. C. Makkar, W. E. Dixon, W. G. Sawyer and G. Hu, "A New Continuously Differentiable Friction Model for Control Systems Design," *Proceedings of the IEEE/ASME International Conference on Advanced Intelligent Mechatronics*, Monterey, CA (2005) pp. 600–605.
36. T. Liu, Y. Inoue and K. Shibata, "A wearable ground reaction force sensor system and its application to the measurement of extrinsic gait variability," *Sensors*, **10**, 10240–10255 (2010).
37. U. Seven, T. Akbas, K. Fidan and K. Erbatur, "Bipedal robot walking control on inclined planes by fuzzy reference trajectory modification," *Soft Comput.* **16**, 1959–1976 (2012).
38. I. Hashlamon and K. Erbatur, "*Experimental Verification of an Orientation Estimation Technique for Autonomous Robotic Platforms*." (Master Istanbul: Sabanci University, 2010).
39. S. Kajita and K. Tani, "Study of Dynamic Biped Locomotion on Rugged Terrain-Derivation and Application of the Linear Inverted Pendulum Mode," *Proceedings of IEEE International Conference on Robotics and Automation*, Sacramento, CA (1991) pp. 1405–1411.
40. K. Erbatur and U. Seven, "Humanoid Gait Synthesis with Moving Single Support ZMP Trajectories," *Proceedings of the 13th Iasted International Conference on Robotics and Applications/Proceedings of the Iasted International Conference on Telematics* (K. Schilling, ed.) (Anaheim: Acta Press Anaheim, Anaheim, 2007) pp. 95–100.
41. I. Hur, Y. Matsuki, N. Tomokuni, J. Huang and T. Yabuta, "Standing Stability of Surfing Robot without Force Sensor," *25th Annual Conference of the Robotics Society of Japan, 3H11*, (2007) pp. 15–18.
42. B. J. Stephens, "State Estimation for Force-Controlled Humanoid Balance using Simple Models in the Presence of Modeling Error," *IEEE International Conference on Robotics and Automation*, Shanghai (2011) pp. 3994–3999.
43. I. Hashlamon and K. Erbatur, "Center of Mass States and Disturbance Estimation for a Walking Biped," *IEEE International Conference on Mechatronics (ICM 2013)*, Vicenza (ITALY), (2013) pp. 248–253.
44. I. Hashlamon and K. Erbatur, "An improved real-time adaptive Kalman filter with recursive noise covariance updating rules," *Turk. J. Electr. Eng. Comput. Sci.* accepted, (2013) pp. 1–17.
45. M. Van Damme, P. Beyl, B. Vanderborght, V. Grosu, R. Van Ham, I. Vanderniepen, A. Matthys and D. Lefeber, "Estimating Robot End-effector Force from Noisy Actuator Torque Measurements," *IEEE International Conference on Robotics and Automation (ICRA)*, Shanghai (2011) pp. 1108–1113.
46. K. Erbatur, U. Seven, E. Taskiran, O. Koca, M. Yilmaz, M. Unel, G. Kiziltas, A. Sabanovic and A. Onat, "SURALP: A New Full-Body Humanoid Robot Platform," *IEEE-Rsj International Conference on Intelligent Robots and Systems*, New York, (2009) pp. 4949–4954.